

Multi-scale Full-orbit Analysis on Phase-space Behavior of Runaway Electrons in Tokamak Fields with Synchrotron Radiation

Yulei Wang,^{1,2} Hong Qin,^{1,3} and Jian Liu^{1,2,*}

¹*School of Nuclear Science and Technology and Department of Modern Physics, University of Science and Technology of China, Hefei, Anhui 230026, China*

²*Key Laboratory of Geospace Environment, CAS, Hefei, Anhui 230026, China*

³*Plasma Physics Laboratory, Princeton University, Princeton, NJ 08543, USA*

Abstract

In this paper, the secular full-orbit simulations of runaway electrons with synchrotron radiation in tokamak fields are carried out using a relativistic volume-preserving algorithm. Detailed phase-space behaviors of runaway electrons are investigated in different dynamical timescales spanning 11 orders. In the small timescale, i.e., the characteristic timescale imposed by Lorentz force, the severely deformed helical trajectory of energetic runaway electron is witnessed. A qualitative analysis of the neoclassical scattering, a kind of collisionless pitch-angle scattering phenomena, is provided when considering the coupling between the rotation of momentum vector and the background magnetic field. In large timescale up to one second, it is found that the initial condition of runaway electrons in phase space globally influences the pitch-angle scattering, the momentum evolution, and the loss-gain ratio of runaway energy evidently. However, the initial value has little impact on the synchrotron energy limit. It is also discovered that the parameters of tokamak device, such as the toroidal magnetic field, the loop voltage, the safety factor profile, and the major radius, can modify the synchrotron energy limit as well as the strength of neoclassical scattering. The maximum runaway energy is also proved to be lower than the synchrotron limit when the magnetic field ripple is considered.

* corresponding author: jliuphy@ustc.edu.cn

I. INTRODUCTION

As a typical multi-scale process, the dynamics of runaway electrons in tokamak has emerged as an important topic in the study of magnetic confined fusion devices. During tokamak experiments, many operation phases, such as fast shutdown, disruptions, and strong current drive, are accompanied by the generation of runaway electrons [1–15]. The collisional friction from the background plasma cannot prevent the acceleration of these energetic electrons if the inductive loop electric field is larger than a critical value [16, 17]. Through the acceleration by the electric field, the velocity of runaway electrons can be sped up to nearly the light speed. Runaway electrons carrying energies from 10 to 100 MeVs have been observed in different experiments [18–21]. Once hitting the plasma-facing components (PFCs), these energetic electrons can damage the tokamak devices badly. Because of the strong relativistic effect, the synchrotron radiation becomes an important ingredient of runaway electron physics. For extremely energetic runaway electrons, their synchrotron radiation loss could be strong enough to balance out the acceleration by the loop electric field. The radiation dissipation then provides runaway electrons an upper bound of energy, i.e., the synchrotron energy limit [22–25]. The typical duration for a runaway electron with low energy (1keV-1MeV) to reach the energy limit has the order of magnitude of one second while the smallest timescale of Lorentz force is 10^{-11} s [24, 26], which means the dynamical behavior of runaway electrons spans about 11 orders of magnitude in timescale. The multi-scale character poses great difficulty to a satisfying physical treatment of runaway dynamics.

Through averaging out the gyro-motion, the gyro-center theory can reduce the span of timescales by about three orders and is used widely in dealing with runaway electron dynamics. Fruitful results of this theory have been accomplished. Considering the gyro-center approximation regardless of the toroidal geometry, one can transfer the full-orbit dynamical equations of runaway electrons to a set of relaxation equations which are much easier to solve theoretically and numerically [24]. By use of relaxation equations, the momentum evolution structure as well as energy limit has been studied in detail under several kinds of dissipations, such as collision, synchrotron radiation, and bremsstrahlung radiation [22, 23, 27]. Meanwhile, the restriction effect of magnetic ripple on the maximum energy has also been discussed in this way [23]. If involving the toroidal geometry, some extra geometry-related

phenomena arise, often dubbed neoclassical effects. The Ware-pinch effect shows an inward drift of trapped orbit [25, 28, 29], while the neoclassical drift provides an outward radial drift velocity of transit runaway orbits [30]. Both of these phenomena reflect the conservation of the toroidal canonical angular momentum. Recently, gyro-center simulations have been equipped with structure-preserving discrete methods and shown better long-term numerical accuracy than traditional methods [24, 25, 31].

Unlike gyro-center theory, the full-orbit analysis can keep entire physical information covering all timescales of runaway dynamics. Especially, a recent full-orbit simulation on runaway electrons has shown that the assumption of gyro-center theory no longer holds in tokamak magnetic field if the runaway electrons are accelerated to several tens of MeVs [26]. Because of the high energy, the change of background magnetic field direction encountered by runaway electrons is significant even within one gyro-period. The violent change of magnetic field causes a full-orbit effect, the collisionless neoclassical pitch-angle scattering, which arises from the toroidal geometry and causes a violent momentum exchange between parallel and perpendicular directions. It also leads to a drift in momentum space and the significant run-up of perpendicular momentum, which provides a new picture of runaway momentum structure. The energy limit is also found to be higher when the full-orbit effect is considered. Therefore, the full-orbit dynamical analysis is vital to obtain reasonable descriptions on runways.

In this paper, we discuss the detailed full-orbit runaway dynamics in views of both small (10^{-11} - 10^{-9} s) and large (1-3s) timescales and analyze the influences of tokamak design parameters on the long-term motion of runaway electrons. A throughout simulation of the multi-timescale behavior of runways requires more than 10^{12} time steps, which is an astronomically big number and cannot be properly implemented by traditional numerical methods. To tackle the global accumulation of coherent errors for such long-term simulation, we follow the method in Ref. [26] and use a relativistic volume-preserving algorithm (VPA) [32]. As a geometric algorithm, the relativistic VPA possesses long-term numerical accuracy and stability [24, 25, 31–41]. The secular full-orbit dynamics of runaway electrons is obtained through directly solving the Lorentz force equations. The synchrotron radiation is included in the physical model, when the collisional force is ignored.

The characteristic timescale imposed by magnetic force reflects the smallest timescale of

runaway dynamics, which can be defined as the gyro-period

$$\mathcal{T}_c = \frac{2\pi\gamma m_0}{eB}, \quad (1)$$

where γ is the Lorentz factor, m_0 is the rest mass of electron, e is the unit charge, and $B = |\mathbf{B}|$ denotes the strength of magnetic field. Although gyro-center theory breaks down for energetic runaways in toroidal geometry, the gyro-period can still be used as an available characteristic parameter for the small timescale. This is because that the failure of the gyrocenter condition is mainly due to the rapid change of the direction of the magnetic field, while B doesn't vary a lot during each gyro-period. The practicability of \mathcal{T}_c can also be analyzed in the view of the rotation operator. We will show that in the gyro-period timescale the trajectory of an energetic runaway electron is elongated both toroidally and poloidally, and the corresponding \mathcal{T}_c will increase to about one twentieth of the transit period. As a result, the local magnetic field witnessed by an energetic runaway electron rotates rapidly, and the norm of magnetic rotation axial vector, namely, $|\boldsymbol{\Omega}_B| = |\mathbf{b} \times \dot{\mathbf{b}}|$, becomes comparable with $1/\mathcal{T}_c$, which leads to the collisionless neoclassical pitch-angle scattering. A qualitative description of the collisionless scattering is given through the coupling between the rotations of momentum and magnetic vector. The momentum drift caused by the long-term accumulation of collisionless scattering effect is analyzed. To be specific, the perpendicular momentum of a runaway electron increases in the direction of $-\boldsymbol{\Omega}_B$ which is approximately in the direction of z-axis.

The long-term evolution of momentum and energy are investigated for runaways with different initial conditions in phase space. Four main characteristics of the momentum evolution structure are discussed: (a) the zero-point position of perpendicular momentum, (b) the oscillation amplitude when reaching energy limit, (c) maximum parallel momentum, and (d) maximum perpendicular momentum. Among these four characteristics, (a) and (b) correspond to the fine oscillating structures of runaway orbit, meanwhile (c) and (d) are related closely to the synchrotron energy limit [26]. It will be shown that the zero-point of perpendicular momentum and the amplitude of oscillation are impacted significantly by the initial pitch-angles. Larger initial perpendicular momentum will cause larger zero-point position and stronger oscillation in small timescale. However, the initial momentum samplings have little influence on the energy limit. The impact of the initial configuration position on the long-term momentum evolution is also negligible. For a deeper insight, we

define two quantities to describe the long-term integral behavior of runaway energies, i.e., the energy loss-gain ratio and the energy balance time. The energy loss-gain ratio is defined as the ratio of the total energy loss through radiation to the energy gained from the loop electric field. This ratio is influenced by the initial runaway momentum significantly but is nearly independent of the initial position. The evolutions of energy loss-gain ratio under different initial phase space samplings have similar behaviors in the vicinity of the energy limit. The energy balance time describes the time required for a new-born runaway electron to run up to its energy limit, which is approximately independent of its initial values in the phase space.

Finally, in order to describe tokamak experimental research on runaways, the influences of tokamak parameters, including the loop electric field, the background magnetic field, the major radius, and the safety factor q , on both the energy limit and the strength of neoclassical pitch-angle scattering are analyzed. Large loop inductive electric field can impel runaways with high energy in short time. On the other hand, the strength of magnetic field mainly contributes to the neoclassical effects. Smaller magnetic field will stall for the energy balance time but bump up the perpendicular momentum more significantly. As a key parameter of tokamaks, the major radius affects the energy limit and the balance time through changing the power of radiation. Smaller major radius results in stronger radiation and shorter balance time. The strength of neoclassical scattering decreases slightly as the growth of major radius. The influence of safety factor is also discussed. Involving several different effects, the maximum energy, the balance time, and the maximum perpendicular momentum roughly depend on the safety factor linearly. When q is small, the dependence of momentum oscillation on q is more sensitive. When q is larger than 2, the amplitude of oscillation approaches to a constant approximately. Lastly, we also study the effect of magnetic field ripple due to the finite number of toroidal coils. The energy limit is proved to be lower than the synchrotron limit when magnetic ripple exists, which is consistent with the theoretical analysis in Ref. [42].

This article is organized as follows. Section II gives an introduction of the physical model and the algorithm used in the numerical research. In Sec. III, the full-orbit behavior of a runaway electron is analyzed in the timescale of \mathcal{T}_c . The long-term evolution behaviors of momentum and energy are studied under different initial phase space samplings in Sec. IV and Sec. V respectively. Section VI focuses on how the parameters of tokamak affect the

energy limit and the neoclassical pitch-angle scattering of runaway electrons. And Sec. VII concludes this paper and our future plans.

II. PHYSICAL MODEL AND NUMERICAL METHOD

The first-principle physical model of runaway electron is the solution of relativistic Lorentz force equations. The synchrotron radiation is included as the dominate channel of runaway energy dissipation. The collisional resistance is neglected because its effect is small enough compared with the collisionless pitch-angle scattering [26]. Consequently, we describe the runaway electrons by use of the following equations,

$$\frac{d\mathbf{x}}{dt} = \mathbf{v}, \quad (2)$$

$$\frac{d\mathbf{p}}{dt} = -e(\mathbf{E} + \mathbf{v} \times \mathbf{B}) + \mathbf{F}_R, \quad (3)$$

$$\mathbf{p} = \gamma m_0 \mathbf{v}, \quad (4)$$

where \mathbf{x} , \mathbf{p} , \mathbf{v} are respectively position, momentum, and velocity of a runaway electron, \mathbf{E} and \mathbf{B} denote electric and magnetic field. The radiation force is defined as [26]

$$\mathbf{F}_R = -P_R \frac{\mathbf{v}}{v^2}, \quad (5)$$

where P_R is the radiation power determined by [43]

$$P_R = \frac{e^2}{6\pi\epsilon_0 c} \gamma^6 \left[\left(\frac{\mathbf{a}}{c} \right)^2 - \left(\frac{\mathbf{v}}{c} \times \frac{\mathbf{a}}{c} \right)^2 \right]. \quad (6)$$

Here, ϵ_0 denotes the permittivity in vacuum, c is the speed of light in vacuum, and $\mathbf{a} = d\mathbf{v}/dt$ is the acceleration vector.

The full-orbit simulation of Eqs. 2-6 is essentially a multi-scale numerical problem. To achieve the omni-timescale dynamics of runaway electron, the minimum time resolution should be less than \mathcal{T}_c , which is typically around 10^{-11} s. However, since the timescale of acceleration process of runaway electrons is one second, hundreds of billions of steps are needed in numerical calculation. Traditional algorithms, such as the fourth-order Runge-Kutta method, can only restrict one-step numerical error. So the global coherent accumulation of numerical errors from such a large number of simulation steps will go far beyond the tolerance of numerical accuracy. To solve the numerical error problem for long-term

simulations, we deal with the problem by use of a relativistic volume-preserving algorithm [32]. The long-term numerical stability and accuracy of the relativistic VPA has been verified. According to the construction of relativistic VPA, the motion equations of runaway electrons are discretized as

$$\mathbf{a}_k = \frac{\mathbf{v}_k - \mathbf{v}_{k-1}}{\Delta t}, \quad (7)$$

$$\mathbf{F}_{Rk} = \mathbf{F}_R(\mathbf{a}_k, \mathbf{v}_k), \quad (8)$$

$$\mathbf{x}_{k+\frac{1}{2}} = \mathbf{x}_k + \frac{\Delta t}{2} \frac{\mathbf{p}_k}{\sqrt{m_0^2 + \mathbf{p}_k^2/c^2}}, \quad (9)$$

$$\mathbf{p}^- = \mathbf{p}_k - e \frac{\Delta t}{2} \mathbf{E}_{k+\frac{1}{2}} + \frac{\Delta t}{2} \mathbf{F}_{Rk}, \quad (10)$$

$$\mathbf{p}^+ = \text{Cay} \left(\frac{-e \Delta t \hat{\mathbf{B}}_{k+1/2}}{2 \sqrt{m_0^2 + \mathbf{p}^{-2}/c^2}} \right) \mathbf{p}^-, \quad (11)$$

$$\mathbf{p}_{k+1} = \mathbf{p}^+ - e \frac{\Delta t}{2} \mathbf{E}_{k+\frac{1}{2}} + \frac{\Delta t}{2} \mathbf{F}_{Rk}, \quad (12)$$

$$\mathbf{x}_k = \mathbf{x}_{k+\frac{1}{2}} + \frac{\Delta t}{2} \frac{\mathbf{p}_{k+1}}{\sqrt{m_0^2 + \mathbf{p}_{k+1}^2/c^2}}, \quad (13)$$

where the subscript, k , denotes the k -th step, Δt is the time interval, $\hat{\mathbf{B}}$ is defined as

$$\hat{\mathbf{B}} = \begin{pmatrix} 0 & B_z & -B_y \\ -B_z & 0 & B_x \\ B_y & -B_x & 0 \end{pmatrix}, \quad (14)$$

and the symbol Cay denotes the Cayley transform [32]. The radiation force is treated as an effective electric field in the discrete equations. In this paper, a typical configuration for tokamak field is used, i.e.,

$$\mathbf{B} = -\frac{B_0 R_0}{R} \mathbf{e}_\xi - \frac{B_0 \sqrt{(R - R_0)^2 + z^2}}{qR} \mathbf{e}_\theta, \quad (15)$$

$$\mathbf{E} = E_l \frac{R_0}{R} \mathbf{e}_\xi. \quad (16)$$

Here we use the cylindrical coordinate system (R, ξ, z) . In Eqs. 15 and 16, \mathbf{e}_ξ and \mathbf{e}_θ are respectively the toroidal and poloidal unit vectors, R_0 is the major radius, q denotes safety factor, E_l is the strength of loop electric field, and B_0 is the magnitude of background magnetic field. The time step of simulation is set as $\Delta t = 1.9 \times 10^{-12} s$, which is about 1% of \mathcal{T}_c .

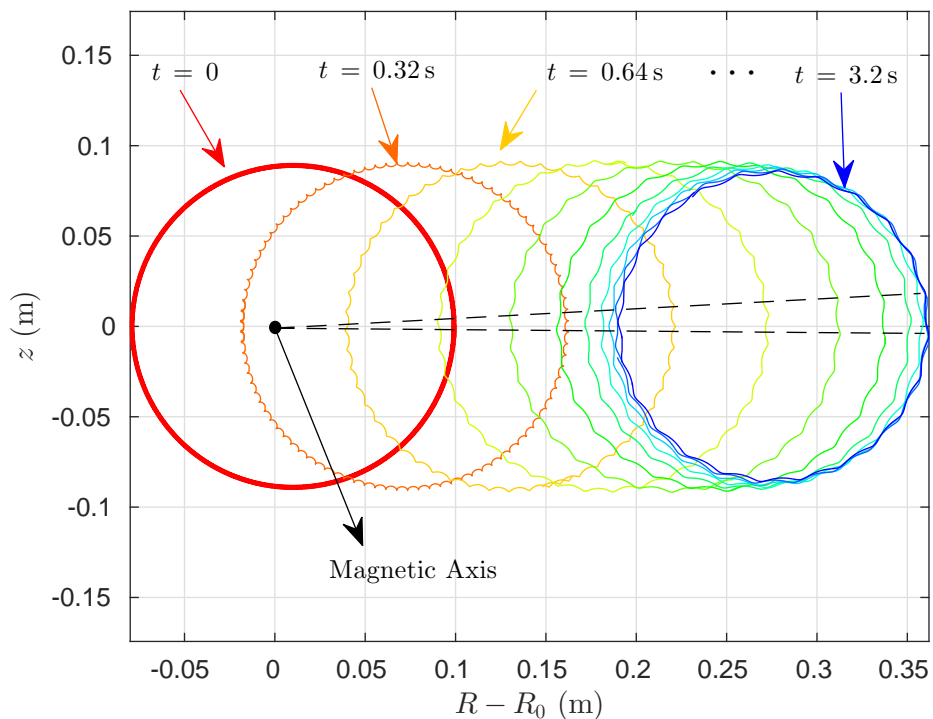


Figure 1. Full-orbit snapshots of runaway orbit projected in the poloidal plane at different moments. The configuration of field is determined by $R_0 = 1.7$ m, $a = 0.4$ m, $q = 2$, $B_0 = 2$ T, and $E_l = 0.2$ V/m. The runaway electron is initially sampled with momentum $p_{\parallel 0} = 5 m_0 c$, $p_{\perp 0} = 1 m_0 c$ at $R = 1.8$ m, $\xi = z = 0$. Besides the neoclassical radial drift, the ripple structures are obviously exhibited. The poloidal angle spanned by one ripple at $t = 3.2$ s is marked by black dashed lines.

III. RUNAWAY DYNAMICS IN \mathcal{T}_c -TIMESCALE

In this section, we offer a straightforward full-orbit picture of runaway electron dynamics in \mathcal{T}_c -timescale. Because it has been proved that the gyro-center model breaks down for the dynamics of energetic runaway electrons [26], the motion of runaways in \mathcal{T}_c -timescale looks quite different from the gyro-center picture. Here we set calculation parameters based on a typical tokamak, that is $R_0 = 1.7$ m, $a = 0.4$ m, $q = 2$, $B_0 = 2$ T, and $E_l = 0.2$ V/m. The initial position is chosen as $R = 1.8$ m, $\xi = z = 0$, and the initial parallel and perpendicular momentums are set as $p_{\parallel 0} = 5 m_0 c$ and $p_{\perp 0} = 1 m_0 c$ respectively.

Figure 1 depicts snapshots of poloidal projection of runaway orbits at different moments. Besides the outward neoclassical drift orbit similar to the results from the gyrocenter code

[25, 30], it can also be observed that there exist ripple structures superimposed on each circle orbit. These fine ripple structures, which cannot be recovered by gyro-center models, correspond to the runaway motion in \mathcal{T}_c -timescale and become more obvious as time going. Accompanying the increase of runaway energy, both the velocity and \mathcal{T}_c of runaway electrons grows. The runaway orbit during each \mathcal{T}_c is elongated both toroidally and poloidally. As shown in Fig.1, the ripple structure becomes more and more evident due to the enhance of the orbit elongation. Because one circular orbit projected in the poloidal plane actually corresponds to a transit period \mathcal{T}_{tr} , the decrease of the ripple structure number with energy increase implies the decrease of $\mathcal{T}_{tr}/\mathcal{T}_c$ and hence the increase of \mathcal{T}_c . For example, at $t = 3.2$ s, there are only about 24 ripples during one poloidal period, which means there are 24 \mathcal{T}_c s in one transit period.

The change of magnetic field witnessed by the runaway electron within one gyro-period has a close relation to the deformation of runaway orbit. The variance of the background magnetic field during \mathcal{T}_c at different time is plotted in Fig.2, indicated by the toroidal rotation angle of magnetic field θ_{BT} , the poloidal rotation angle of magnetic field θ_{BP} , the change rate of magnetic strength D_B , and the relative increment of magnetic vector Λ_B . The definition $D_B(t) = (|\mathbf{B}(t + \mathcal{T}_c)| - |\mathbf{B}(t)|) / |\mathbf{B}(t)|$ reflects relative change of magnetic strength within one gyro-period. The relative increment of magnetic vector during one gyro-period is defined as $\Lambda_B(t) = |\mathbf{B}(t + \mathcal{T}_c) - \mathbf{B}(t)| / |\mathbf{B}(t)|$, which includes the change of direction of the magnetic field. According to Fig.2c, during each gyro-period the increment of the magnetic strength $D_B(t)$, which reflects the small radial size of the ripple structure, is rather small compared with $\Lambda_B(t)$. The poloidal and toroidal rotation angles of magnetic field, θ_{BP} and θ_{BT} , can be approximately expressed by the poloidal and toroidal angles spanned by a single ripple structure. The dashed lines in Fig.1 shows that the maximum poloidal angle spanned by a ripple is about 6° , which is consistent with the result in Fig.2b. Compared with θ_{BP} , θ_{BT} is significantly larger, see Fig.2a. The runaway electron runs about 720° in the toroidal direction and 360° in the poloidal direction within one transit period if $q = 2$. Then at $t = 3.2$ s, 24 ripples appearing in one transit period means that each ripple structure covers about 30° in the toroidal direction, which is consistent with the maximum θ_{BT} in Fig.2a. Therefore, we can conclude that the violent change of magnetic field in \mathcal{T}_c timescale is dominated by its toroidal rotation.

When analyzing the dynamics in the momentum space, one can treat the effect of mag-

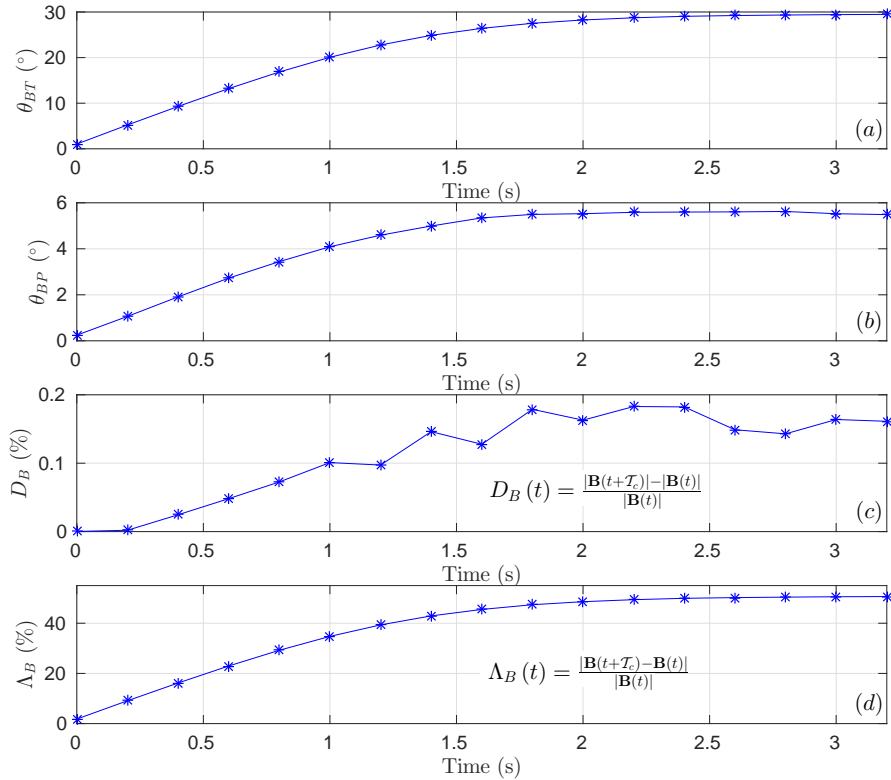


Figure 2. The \mathcal{T}_c timescale increment of \mathbf{B} at different moments when the position of particle is near $z = 0$. (a) depicts the toroidal rotation angle θ_{BT} , (b) gives the poloidal rotation angle θ_{BP} , (c) shows the relative change of magnetic strength $D_B(t)$, and (d) depicts the relative increment of magnetic vector $\Lambda_B(t)$. The maximum toroidal rotation angle of the magnetic field in one gyroperiod is 30° , which is much larger than the corresponding poloidal rotation angle. The increment of strength B is too small to take effect as well. Therefore, the change of magnetic field Λ_B in \mathcal{T}_c timescale is mainly due to the directional change of the magnetic field torodically.

netic field as a rotation operation due to the formation of Lorentz force [33]. The unit magnetic vector $\mathbf{b} = \mathbf{B}/B$ determines the axis of instantaneous momentum rotation, while the magnetic strength B reflects the velocity of rotation as well as the value of \mathcal{T}_c . If \mathbf{b} is approximately a constant in \mathcal{T}_c , the track of \mathbf{p} spans a symmetric cone around \mathbf{b} , see Fig. 3a. However, if the characteristic variation time of \mathbf{b} is comparable with \mathcal{T}_c , the rotations of \mathbf{b} and \mathbf{p} are coupled, see Fig. 3b, where $\boldsymbol{\Omega}_B$, satisfying $|\boldsymbol{\Omega}_B| \sim 1/\mathcal{T}_c$, denotes the rotation axial vector of \mathbf{b} . Therefore, the runaway's pitch-angle undergoes significant change even in the

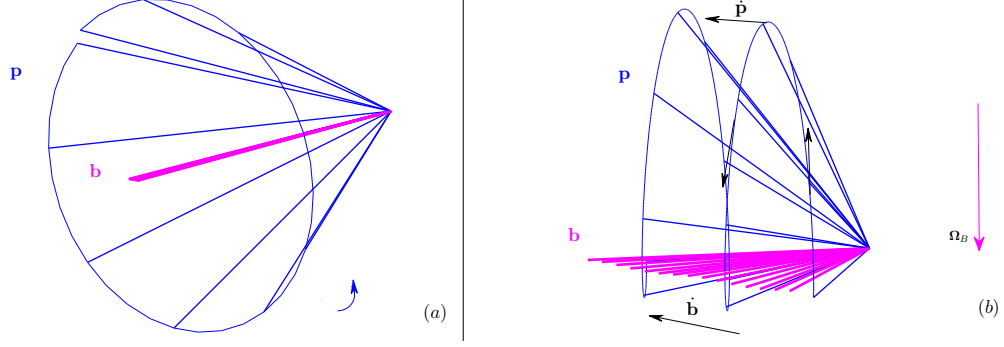


Figure 3. Schematic diagram for the coupling between the rotations of momentum and magnetic vector. The track of momentum vector spans a symmetric cone around \mathbf{b} if the magnetic field changes little in the timescale of \mathcal{T}_c (a). If the rotation rate of \mathbf{b} is comparable to $1/\mathcal{T}_c$, the gyrocenter assumption breaks, and the track of momentum tiles upwards with respect to the magnetic rotation plane (b). The rotation vector of \mathbf{b} is marked by Ω_B , $\dot{\mathbf{b}}$ denotes $d\mathbf{b}/dt$, and $\dot{\mathbf{p}}$ is $d\mathbf{p}/dt$.

timescale of \mathcal{T}_c . In Fig. 3b, $\dot{\mathbf{p}}$ and $\dot{\mathbf{b}}$ are marked using black arrows, where the dot on physical quantities denotes total derivative with respect to time. For runaway electrons carrying negative electric charge, \mathbf{p} always rotates counterclockwise with respect to \mathbf{b} . The purple trails of \mathbf{b} in Fig. 3b establish the rotation plane of \mathbf{b} . It is readily to see that the value of $\dot{\mathbf{p}} \cdot \dot{\mathbf{b}}$ is positive above the plane and negative under the plane. The coupling between the rotations of \mathbf{b} and \mathbf{p} results in asymmetric distribution of perpendicular momentum on two sides of magnetic rotation plane, namely, the average of perpendicular momentum is larger when $\dot{\mathbf{p}} \cdot \dot{\mathbf{b}} > 0$. Equivalently, the rotating momentum can be regarded as being tilting towards the direction of $-\Omega_B$, i.e., the average $\langle \mathbf{p}_\perp \cdot (-\mathbf{e}_{rot}) \rangle$ always increases, where $\mathbf{e}_{rot} = \Omega_B / |\Omega_B|$ is the direction of rotation axial vector, and the bracket denotes the averaging operation over \mathcal{T}_c . On the contrary, a runaway positron carrying positive electric charge always rotates around \mathbf{b} clockwise. Consequently, the runaway positron's momentum tilts towards the direction of Ω_B , namely $\langle \mathbf{p}_\perp \cdot \mathbf{e}_{rot} \rangle$ increases. In the case of our simulation, the toroidal component of magnetic field directs to $-\mathbf{e}_\xi$. Therefore, if neglecting the poloidal component of \mathbf{b} , which is relative small, we have $\mathbf{e}_{rot} = -\mathbf{e}_z$ approximately. Then the average value of z -component of perpendicular momentum $\langle \mathbf{p}_\perp \cdot \mathbf{e}_z \rangle$ keeps growing. This effect is enhanced when the rotation of \mathbf{b} becomes more rapid within one gyro-period. This theoretical analysis agrees with the numerical results in Ref. [26] and offers a direct description of the origin of

collisionless pitch-angle scattering.

IV. SECULAR EVOLUTION OF RUNAWAY MOMENTUM

Due to the collisionless neoclassical scattering, the temporal evolution of runaway momentum shows strong oscillation in small timescale and bumps up in large timescale. The structure of momentum evolution exhibits complex multi-scale characteristics, which is different from the results of gyro-center model. In this section, we aim to find the dependence of the long-term momentum structure on the initial conditions of runaway electrons in the phase space. The setup of tokamak parameters are the same as those in Sec. III.

A typical momentum evolution structure is plotted in the momentum space, where the abscissa is the parallel momentum p_{\parallel} and the ordinate is the perpendicular momentum p_{\perp} , see Fig. 4. The runaway electron starts from $p_{\parallel 0} = 5 m_0 c$ and $p_{\perp 0} = 1 m_0 c$. In the beginning, the oscillation amplitude increases significantly. Then the perpendicular momentum touches 0 at a zero-point $(p_{\parallel zp}, 0)$ due to the oscillation broadening. After passing the zero-point, the global evolution of the momentum curve inclines to the ordinate, which means the rapid increase of the perpendicular momentum. Finally, once the loop electric field is balanced out by the radiation, the momentum band ceases near $p_{\parallel max}$, with obvious oscillation in p_{\perp} and negligible oscillation in p_{\parallel} . The p_{\perp} marked by the purple circle in Fig. 4 corresponds to the synchrotron energy limit. According to Fig. 4, the complete momentum-space structure of runaway evolution can be basically established by four principal parameters, that is the zero-point value of parallel momentum $p_{\parallel zp}$, the oscillation amplitude of perpendicular momentum near the energy limit A_{sp} , the maximum parallel momentum $p_{\parallel max}$, and the average maximum perpendicular momentum $p_{\perp max}$. Among them, $p_{\parallel zp}$ and A_{sp} reflects the nature of momentum oscillation and collisionless pitch-angle scattering, and $p_{\parallel max}$ and $p_{\perp max}$ provide the information of the energy limit [26].

Different initial conditions of runaway electrons in the momentum space mainly alter the position of zero-point and the amplitude of oscillation, i.e., the properties of the neoclassical scattering, but have little impact on the maximum momentum and energy limit. In Fig. 5, we calculate the dependencies of key momentum structure parameters, i.e., (a) $p_{\parallel zp}$, (b) A_{sp} , (c) $p_{\parallel max}$, and (d) $p_{\perp max}$, on initial conditions in the momentum space, under different initial kinetic energies and initial pitch-angles. The two sampling initial kinetic energy values

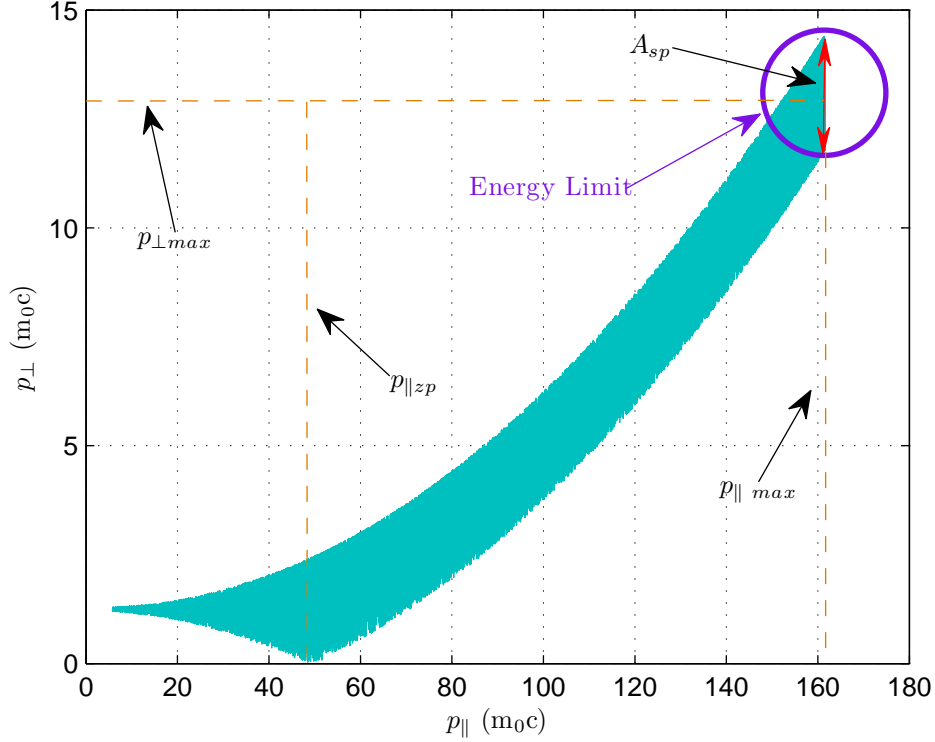


Figure 4. A typical momentum evolution structure is plotted in the momentum space, where the abscissa is the parallel momentum p_{\parallel} and the ordinate is the perpendicular momentum p_{\perp} . The initial momentum is set as $p_{\parallel 0} = 5 m_0c$ and $p_{\perp 0} = 1 m_0c$, and the initial configuration position is $R = 1.8 \text{ m}$, $\xi = z = 0$. The parameters of the magnetic field are given by $R_0 = 1.7 \text{ m}$, $a = 0.4 \text{ m}$, $q = 2$, $B_0 = 2 \text{ T}$, and $E_t = 0.2 \text{ V/m}$. The momentum-space structure of runaway evolution can be established by four principal parameters, that is the value of parallel momentum at zero-point $p_{\parallel zp}$, the limit oscillation amplitude A_{sp} , the maximum parallel momentum $p_{\parallel max}$, and the average maximum perpendicular momentum $p_{\perp max}$.

are chosen as $K_0 = 2.5 \text{ MeVs}$ and $K_0 = 12.5 \text{ MeVs}$. The initial pitch-angles are uniformly sampled from 0 to π in the range $[-1, 1]$. The negative value of $p_{\parallel 0}$ means that the runaway electron initially travels opposite to the electric acceleration direction, i.e., the backward runaways [15, 44]. The effect of initial gyro-phase is not counted in considering the gyro-symmetry in the low energy range. According to Fig. 5a, the value of parallel momentum at zero-point is sensitive to the initial pitch-angle. It is readily to see that the value of parallel momentum at zero-point tends to its initial value, i.e., $p_{\parallel zp} \rightarrow p_{\parallel 0}$, in the small

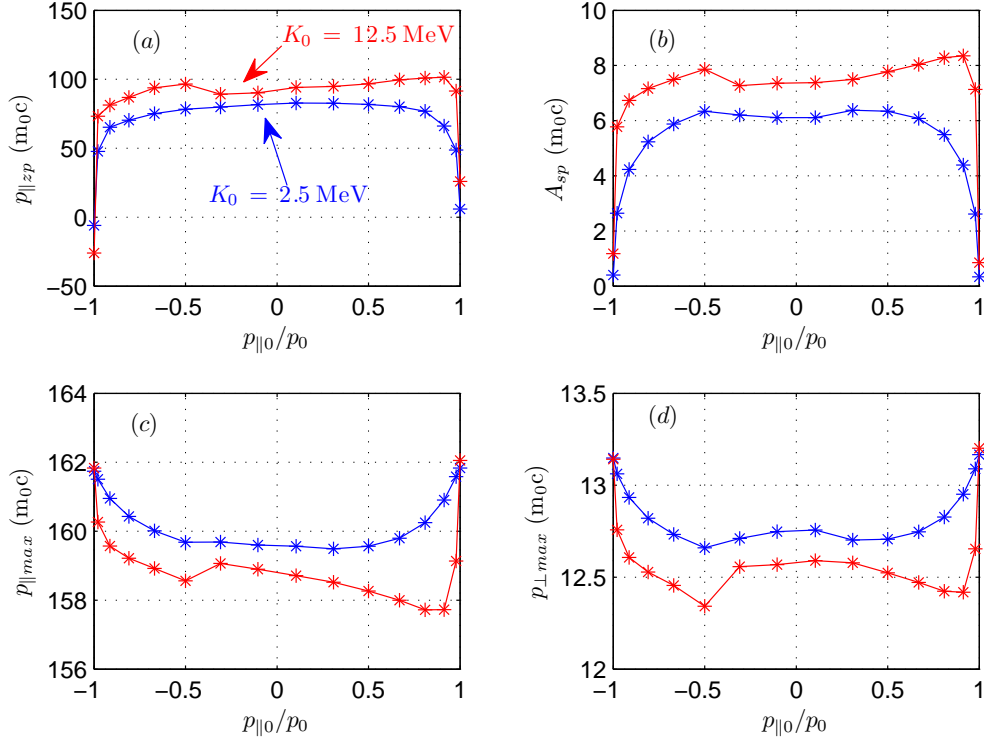


Figure 5. Dependencies of key momentum structure parameters, i.e., (a) $p_{\parallel zp}$, (b) A_{sp} , (c) $p_{\parallel max}$, and (d) $p_{\perp max}$, on initial conditions in the momentum space in terms of the initial kinetic energy and initial pitch-angle. The pitch angle is expressed by $p_{\parallel 0}/p_0$ ranging from -1 to 1, and the two initial kinetic energy values $K_0 = 2.5$ MeVs and $K_0 = 12.5$ MeVs are chosen. The initial position is set to $R = 1.8$ m, $\xi = z = 0$. The parameter of field is given by $R_0 = 1.7$ m, $a = 0.4$ m, $q = 2$, $B_0 = 2$ T, and $E_l = 0.2$ V/m. .

pitch-angle limit $p_{\parallel 0}/p_0 \rightarrow \pm 1$. With the increase of $p_{\perp 0}$, or the decrease of $|p_{\parallel 0}/p_0|$, the value of parallel momentum at zero-point moves toward the positive direction of p_{\parallel} . On the other hand, higher K_0 results in larger $p_{\parallel zp}$. The oscillation amplitude of the momentum structure is also closely related to initial momentum, see Fig. 5b. The amplitude A_{sp} grows with the decrease of absolute value of $p_{\parallel 0}/p_0$ and the increase of initial energy. Especially, if the initial pitch-angle is large enough, the oscillation amplitude may catch up to one half of the maximum perpendicular momentum, see Fig. 5b and Fig. 5d. Conversely, as shown in Fig. 5c and Fig. 5d, the initial momentum has relatively little effect on $p_{\parallel max}$ and $p_{\perp max}$. The relative variations resulted from different $p_{\parallel 0}/p_0$ or K_0 are only about 5% or less.

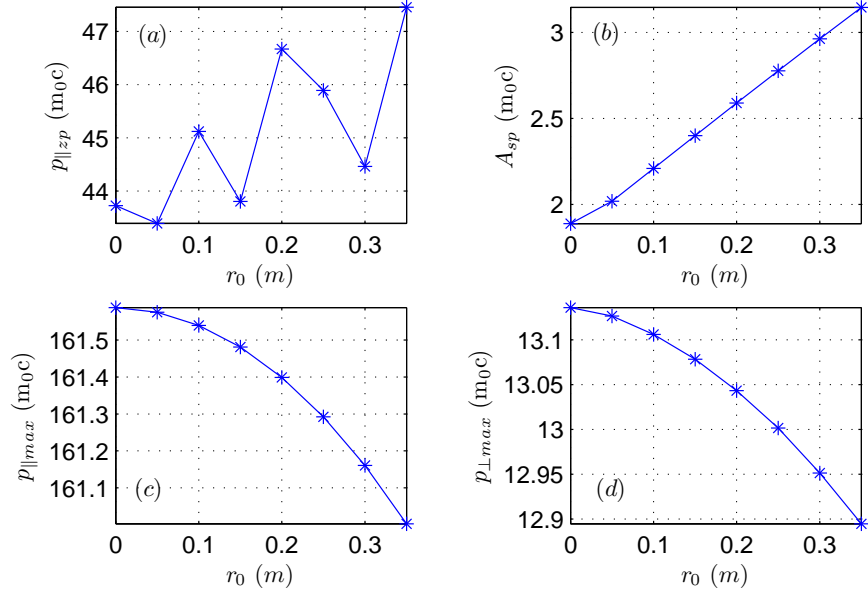


Figure 6. Dependencies of key momentum structure parameters, i.e., (a) $p_{||zp}$, (b) A_{sp} , (c) $p_{||max}$, and (d) $p_{\perp max}$, on different initial samplings of radial position. The initial momentum is set as $p_{||0} = 5 m_0c$ and $p_{\perp 0} = 1 m_0c$, and the initial position is $R = 1.8 m$, $\xi = z = 0$. The configuration of field is given by $R_0 = 1.7 m$, $a = 0.4 m$, $q = 2$, $B_0 = 2 T$, and $E_l = 0.2 V/m$.

The influence of initial positions in the configuration space on the momentum evolution is negligible, as shown in Fig. 6. Since the initial position samplings possess approximate symmetry in both toroidal and poloidal directions, the initial positions of runaway electrons are sampled densely on radial positions. Here r_0 denotes the radial component of toroidal coordinates. The relative variation of $p_{||zp}$ is less than 6% for different initial radial positions in the range $r_0 \in [0, 0.35]$. For larger r_0 , both the electric field and the magnetic field witnessed by a runaway electron are smaller when the transit orbit drifts away from the magnetic axis. So less energy is delivered to runaway electrons from electric field with the increase of r_0 . We can see from Figs. 6c and 6d that $p_{||max}$ and $p_{\perp max}$ decrease slightly when r_0 gets larger, but their relative variations are small. At the same time, because smaller magnetic field implies stronger collisionless scattering [26], the oscillation amplitude of momentum is proportional to r_0 , which is reflected in the plot of A_{sp} in Fig. 6b.

V. INTEGRAL ATTRIBUTES OF ENERGY EVOLUTION

In this section, we focus on two important attributes of energy evolution, namely, the energy loss-gain ratio and the energy balance time. The energy loss-gain ratio of runaway electrons is defined as the ratio of the energy dissipation through radiation to the energy gained from the loop electric field. The energy balance time describes the time required by a low-energy runaway electron from its birth to reaching the energy limit. Unlike the energy limit, which can be analyzed through the stable point of a dynamical system, the energy loss-gain ratio and the energy balance time involves integral quantities over full orbits. Since it is too difficult to analytically calculate the integrations for multi-timescale dynamics of runaway electrons in tokamak fields, long-term numerical integration turns out to be the only practical way to achieve the accurate loss-gain ratio and energy balance time. The parameters of tokamak we use in this section are the same as those in Sec. III.

A. Energy loss-gain ratio

The energy loss-gain ratio is defined as

$$\mathcal{R}_{lg}(t) = \frac{L_s(t)}{L_s(t) + G_E(t)}, \quad (17)$$

where $L_s(t) = \left| \int_0^t \mathbf{F}_R \cdot d\mathbf{x} \right|$ is the energy loss from the synchrotron radiation, and $G_E(t) = \int_0^t \mathbf{E} \cdot d\mathbf{x} - L_s$ is the net runaway energy gained from electric field. After a runaway electron reaches its energy limit, $G_E(t)$ becomes a constant which is expressed using the symbol G_E^m . Therefore, the energy loss-gain ratio has a simple form at energy limit, namely,

$$\mathcal{R}_{lg}^m(t) = \frac{L_s(t)}{L_s(t) + G_E^m}. \quad (18)$$

In Fig. 7, the evolution of \mathcal{R}_{lg} is plotted with different initial pitch-angles, kinetic energy, and radial positions. From Fig. 7a and Fig. 7b, we can see that the initial pitch-angle and energy mainly influence \mathcal{R}_{lg} at the early stage of acceleration. Larger pitch-angle means smaller parallel velocity, which hence results in weaker electric acceleration power and stronger radiation through perpendicular motion. The increase of initial energy will enhance the radiation. Therefore, \mathcal{R}_{lg} grows together with the increase of θ_p and K_0 . On the other hand, according to Fig. 7c, the impact of initial radial position on the behavior of \mathcal{R}_{lg} is

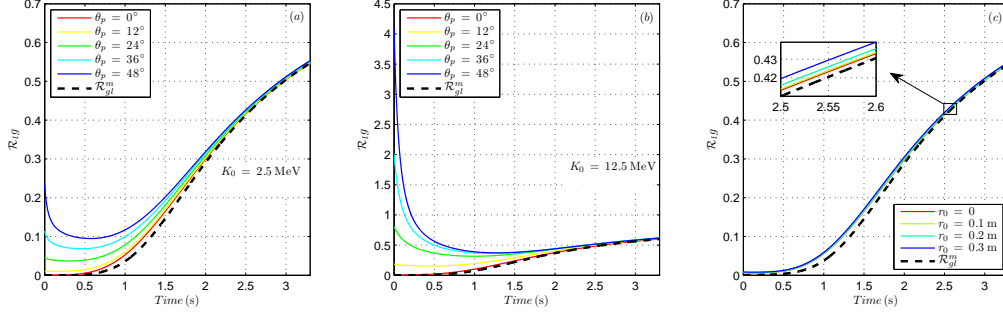


Figure 7. The evolution of energy loss-gain ratio \mathcal{R}_{lg} under different initial energies, pitch-angles, and radial positions. Subfigures (a) and (b) show the evolution of \mathcal{R}_{lg} for $K_0 = 2.5 \text{ MeV}$ and 12.5 MeV respectively. The initial pitch-angles in (a) and (b) are chosen as $\theta_p = 0^\circ, 12^\circ, 24^\circ, 36^\circ, 48^\circ$. In (c), the initial radial position varies from 0 to 0.3 m while the initial momentum is set as $p_{\parallel 0} = 5 m_0 c$ and $p_{\perp 0} = 1 m_0 c$. The influence of r_0 on evolution of \mathcal{R}_{lg} is negligible, and a zoomed-in window showing the details of these curves is embeded in (c) to give a detailed presentation. The dashed curves in all subfigures are reference lines determined by $\mathcal{R}_{lg}^m(t)$, which are calculated using the initial pitch angle $\theta_p = 0^\circ$ in subfigures (a) and (b) and using the initial radial position $r_0 = 0$ in (c).

very weak. All the curves in Fig. 7 asymptotically approach to the reference line of \mathcal{R}_{lg}^m after 3 s. Therefore the initial position and momentum of runaways has little effect on the energy loss-gain ratio after reaching the energy limit, when about 55% of the electric energy has been radiated.

B. Energy balance time

We now focus on how long it takes for a runaway electron to reach its energy limit, i.e., the energy balance time t_{blc} . To calculate t_{blc} , the start point and end point of acceleration process should be determined. The end point is defined as the moment when the loop electric field is balanced by the synchrotron radiation. At this time, because of the neoclassical pitch-angle scattering, physical quantities, such as momentum, electric acceleration power, and radiation power, show strong oscillations in the gyro-period timescale. The electric field is balanced out by the radiation loss only in the sense of long-term average. Therefore, we

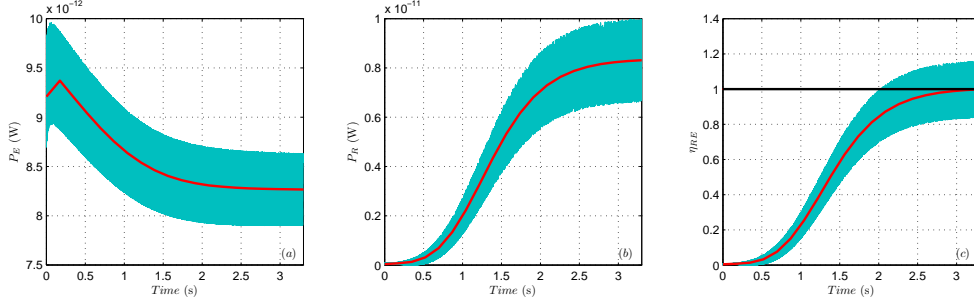


Figure 8. Typical evolution curves of (a) electric acceleration power P_E , (b) radiation power P_R , and (c) the average loss-gain power ratio η_{RE} . The green bands denote the full-orbit evolution curves including fine timescale oscillations. The red curves denote the results after averaging over one transit period.

define the average loss-gain power ratio as

$$\eta_{RE} = \left\langle \frac{P_R}{P_E} \right\rangle_{trans}, \quad (19)$$

where $P_R = |\mathbf{F}_R \cdot \mathbf{v}|$ is the radiation power, $P_E = \mathbf{E} \cdot \mathbf{v}$ is the electric acceleration power and the bracket $\langle \dots \rangle_{trans}$ means the average over a transit period. Then it is convenient to define the end point of t_{blc} as the moment when $\eta_{RE} = 1$. The end point of t_{blc} can also be inferred from the relative behavior of \mathcal{R}_{lg} and \mathcal{R}_{lg}^m . Because the evolutionary trend of \mathcal{R}_{lg} becomes the same as that of \mathcal{R}_{lg}^m after reaching energy limit, the moment when the curves of \mathcal{R}_{lg} and \mathcal{R}_{lg}^m begin to overlap also indicates the finish of acceleration.

The settlement of the start point of t_{blc} , however, is more complex since runaway electrons are born with different phase-space states and origins. There is even not a clear criterion for the emergence of a single runaway electron because of its statistical essence. Fortunately, it can be verified that different initial energies matters little to the energy balance time for runaways under several MeVs. The typical electric field can accelerate a low-energy runaway electron to several MeVs within 10% t_{blc} [26]. In this paper, we set the start-up energy of a runaway electron as 2.1 MeV. The arbitrariness of the setup of the start-up energy has small impact on the value of t_{blc} within the range of several MeVs. According to Fig. 7, it can also be observed that different initial samplings in phase space has little effect on t_{blc} .

The typical evolutions of P_E , P_R , and η_{RE} are plotted in Fig. 8. All of these curves show strong oscillations. The transit-period average values are plotted using the red curves. The power of electric acceleration increases at the beginning because of the growth of runaway

velocity. Once the runaway speed is close enough to c , the electric acceleration power is dominated by the strength of the loop electric field. Since the electric field is inversely proportional to radial position, P_E decreases accompanied by the outward drift of runaway transit orbits, see Fig. 8a. The radiation power monotonously increases with the runaway energy accompanied by stronger oscillations, see Fig. 8b. The red curve in Fig. 8c is a typical evolution of η_{RE} , which reflects that the loss-gain rate power ratio climbs steeply in the midterm of runaway acceleration. The energy balance time is around 3 s in this case.

VI. INFLUENCES OF TOKAMAK DEVICE PARAMETERS

Many experiments have confirmed the existence of runaway electrons with energies ranging from 10-100 MeVs in tokamak devices[45–47]. To describe and further understand the experimental results, it is necessary to study the dependence of runaway dynamical properties on the device parameters. In this section several characteristics of runaways, which may be experimentally diagnosed directly or indirectly, such as the maximum energy E_{max} , the energy balance time t_{blc} , the oscillation amplitude of perpendicular momentum near the energy limit A_{sp} , and the average maximum perpendicular momentum $p_{\perp max}$, are discussed. The influences from three key tokamak device parameters are considered, including the strength of tokamak field, the major radius, and the safety factor. The impact of magnetic field ripple is also studied through full-orbit simulations.

As vital design parameters, the intensities of equilibrium tokamak fields are reflected in E_l and B_0 . The toroidal curvature of fields is determined by the major radius R_0 , while the poloidal curvature is reflected in the safety factor q . All these parameters influence the energy limit and collisionless pitch-angle scattering by stepping in different aspects of runaway dynamics, such as the acceleration, the synchrotron radiation, and the change rate of magnetic field during each gyro-period. Larger E_l leads to stronger acceleration, while increasing B_0 results in the mitigation of collisionless pitch-angle scattering. The increase of magnetic curvature corresponds to the enhancement of radiation and toroidal effect. Considering the loop electric field \mathbf{E} and toroidal magnetic \mathbf{B} decreases radially, the neoclassical drift velocity, approximately given by qE_l/B_0 [25, 30], also interferes the energy limit rule and the neoclassical scattering process. The change of one single device parameter thus may affect the runaway dynamics in several interactional mechanisms. On the other

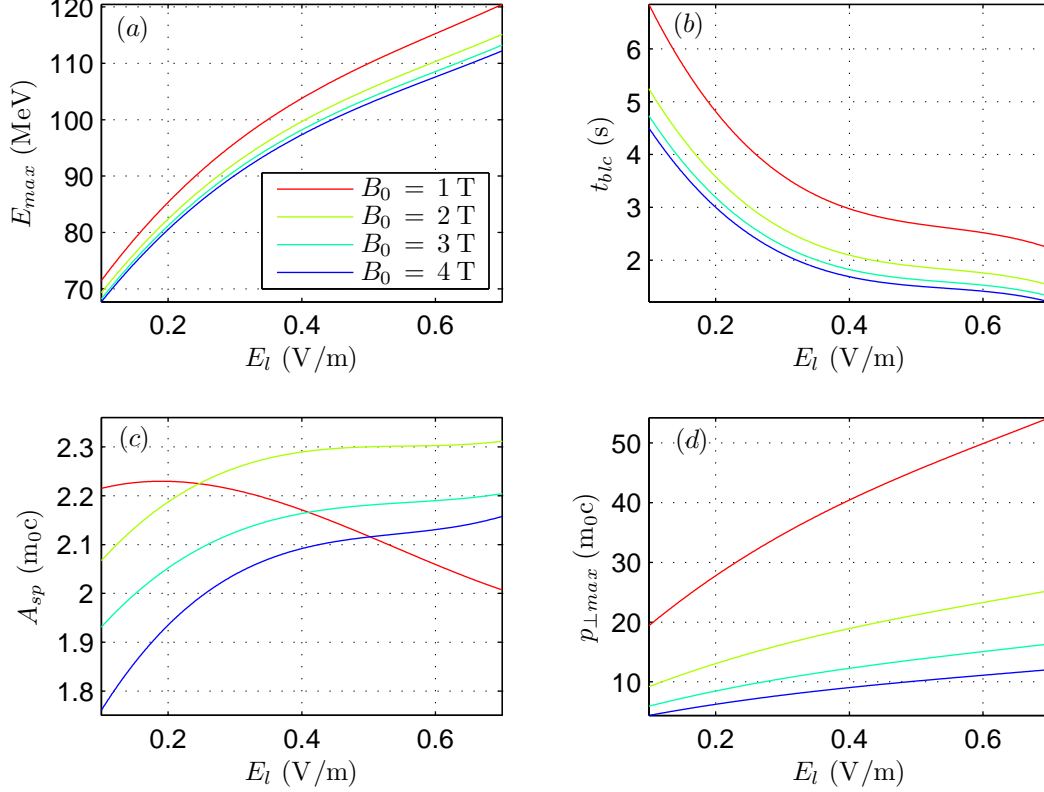


Figure 9. The plots of (a) the maximum energy of a runaway electron, (b) the energy balance time, (c) the oscillation amplitude at energy limit, and (d) the maximum perpendicular momentum against loop electric field with different magnetic field strengths. The initial condition is set to $p_{\parallel 0} = 5 m_0c$, $p_{\perp 0} = 1 m_0c$, $R = 1.8$ m, and $\xi = z = 0$. The major radius of tokamak is $R_0 = 1.7$ m, and the safety factor is $q = 2$.

hand, the magnetic field ripple can also impose stochastic instability to runaway dynamics through the nonlinear resonance, which restricts the maximum runaway energy below the synchrotron limit [42]. In this section, the initial conditions are sampled in the phase space the same as in Sec. III.

A. Influences of field strength

Figure 9 summarizes the influences from E_l and B_0 on E_{max} , t_{blc} , A_{sp} , and $p_{\perp max}$. Curves with different colors correspond to different central magnetic field strength. The major

radius is set as 1.7 m and the safety factor is 2. In tokamak experiments, the loop electric field has the strongest impact on the runaway energy limit. During disruptions the energy of plasma is released through a strong inductive loop electric field. According to Figs. 9a and 9b, the runaways can reach higher energy limits in shorter time when the loop electric field increases, thus posing more severe threat in major disruption.

On the other hand, the energy limit also depends on the magnetic field significantly. From Fig. 9a, we can see that the energy limit is higher for smaller B_0 . It can be noticed that the increment of E_{max} due to the drop of B_0 is smaller than the result in Ref. [26] which assumes a uniformly distributed electric field in the radial direction. The difference is caused by the neoclassical drift and radial distribution of electric field. For smaller B_0 , as the neoclassical drift is faster, the electric field witnessed by runaway electrons decreases faster. Therefore, the energy limit is reduced by several MeVs compared with that in the uniform electric field distribution. This mechanism also results in longer balance time, see Fig. 9b.

The strength of tokamak fields has small effects on the oscillation amplitude in small timescale, see Fig. 9c. The largest relative change of oscillation amplitude caused by tokamak field is about 10%. However, according to Fig. 9d, the ramp-up of perpendicular momentum in large timescale can be altered significantly by adjusting the strength of tokamak field. The growth rate of $p_{\perp max}$ versus loop electric field becomes much larger for smaller magnetic field. This embodies stronger accumulation of neoclassical pitch-angle scattering on perpendicular runaway momentum, also more violent deviation from gyro-center model, for smaller magnetic field and large electric field.

B. Influences of Major Radius

Next-generation tokamak devices possess larger major radius to achieve higher operation parameters. For example, the major radius of ITER is designed to be 6.2 m. Larger tokamaks have better confinement on fusion plasma as well as runaway electrons. More energy may release through runaway currents during major disruptions. It is obvious that runaway electron can gain more energy from the stronger electric field. On the other hand, we will show that, even with the same strength of electric field, the change of major radius R_0 will influence the energy limit rule and the neoclassical pitch-angle scattering directly. In this part, the tokamak field is set as $E_l = 0.2 \text{ V/m}$ and $B_0 = 2 \text{ T}$, and the safety factor is 2.

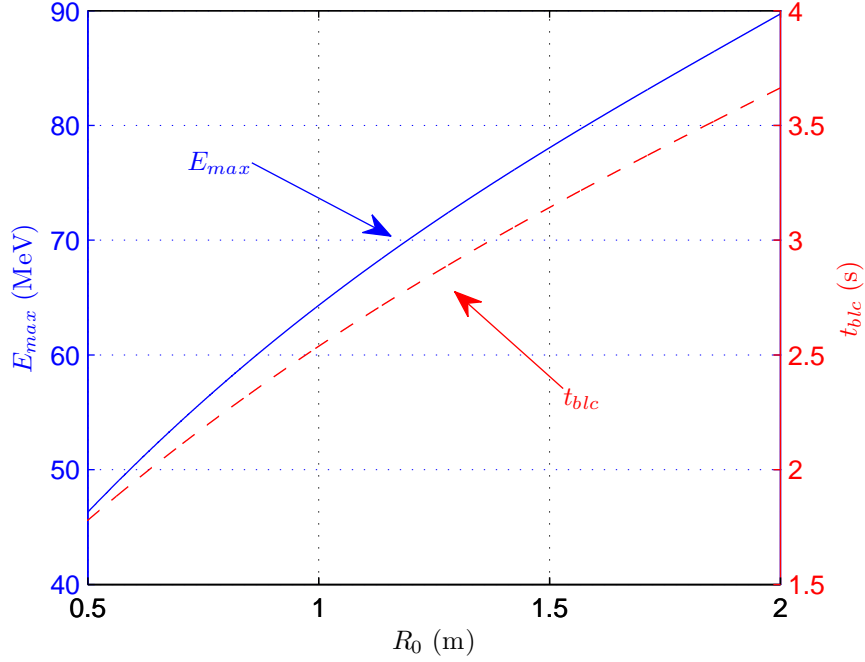


Figure 10. The plots of energy limit E_{max} , denoted by the blue solid curve and the left ordinate, and the energy balance time t_{blc} , denoted by the red dashed curve and the right ordinate, against the major radius. The initial condition of runaway electron in phase space is sampled as $p_{\parallel 0} = 5 m_0 c$, $p_{\perp 0} = 1 m_0 c$, $R = 1.8$ m, and $\xi = z = 0$. The tokamak field is set as $E_l = 0.2$ V/m and $B_0 = 2$ T, and the safety factor is chosen as $q = 2$.

Figure 10 plots the energy limit and the balance time against different major radius. We can see that both the maximum energy and balance time increase proportional to the major radius R_0 approximately, because the synchrotron radiation closely depends on the curvature of the runaway orbit [22]. Smaller R_0 brings larger toroidal curvature and thus stronger radiation power. The runaway electrons have stronger synchrotron dissipation in small devices. As a result, their energy limit is lower and energy balance time t_{blc} is shorter.

The curvature of tokamak field reflects the significance of toroidal geometry. So the major radius also affects the collisionless pitch-angle scattering evidently. For devices with smaller major radius and larger toroidal curvature, the same distance traveled in toroidal direction brings more variation of the magnetic field direction. Consequently, the assumption of gyro-center model breaks down easier in smaller devices. As expected, the magnitude of oscillation at energy limit A_{zp} and the maximum perpendicular momentum $p_{\perp max}$ drop with

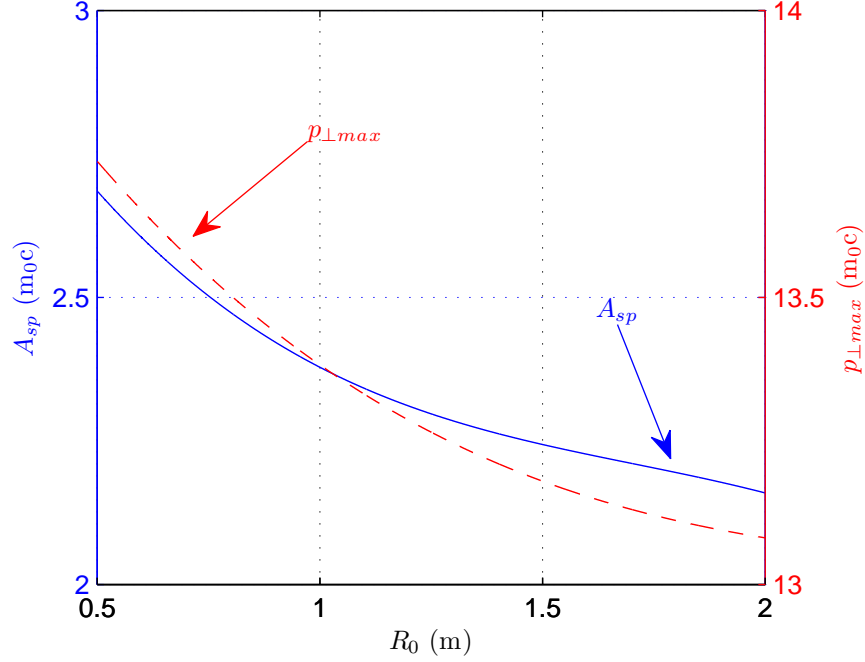


Figure 11. The plots of magnitude of oscillation at energy limit A_{zp} , denoted by the blue solid curve and the left ordinate, and the maximum perpendicular momentum $p_{\perp max}$, denoted by the red dashed curve and the right ordinate, against the major radius. The initial condition of runaway electron in phase space is sampled as $p_{\parallel 0} = 5 m_0c$, $p_{\perp 0} = 1 m_0c$, $R = 1.8$ m, and $\xi = z = 0$. The tokamak field is set as $E_t = 0.2$ V/m and $B_0 = 2$ T, and the safety factor is $q = 2$.

the increase of R_0 , see Fig. 11.

C. Influences of safety factor

The safety factor q is another important parameter of tokamaks, which reflects the geometric character of magnetic surface. Smaller q corresponds to stronger poloidal magnetic field and more poloidal periods the magnetic line winding during each toroidal cycle. The curvature of magnetic line is determined toroidally by the major radius and poloidally by q . Therefore, dynamical processes related to geometry configurations, such as synchrotron radiation and the neoclassical pitch-angle scattering, will be influenced by q . Larger poloidal field also brings more difficult for electric field to accelerate the runaway electrons toroidally. Meanwhile, the value of q also influence the neoclassical drift and thus the change of the local

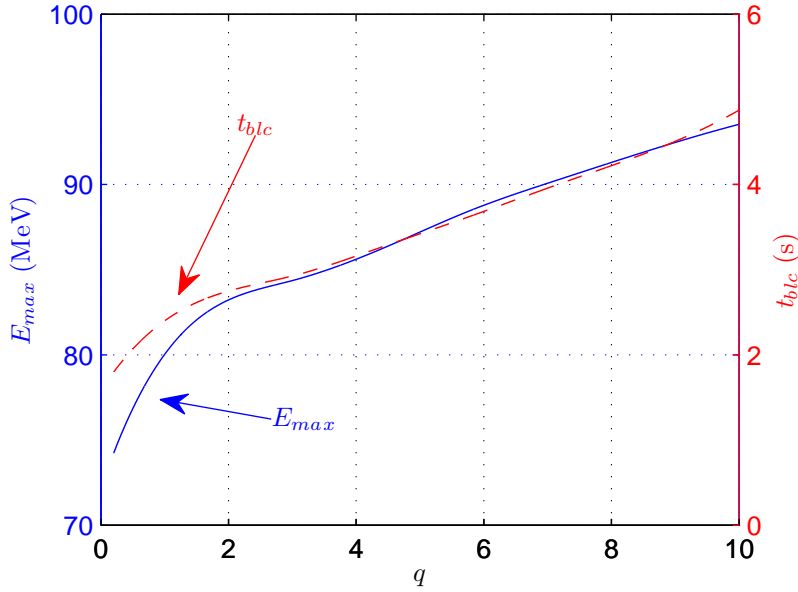


Figure 12. The plots of energy limit E_{max} , denoted by the blue solid curve and the left ordinate, and the energy balance time t_{blc} , denoted by the red dashed curve and the right ordinate, against safety factor. The initial condition of runaway electron in phase space is sampled as $p_{\parallel 0} = 5 m_0 c$, $p_{\perp 0} = 1 m_0 c$, $R = 1.8$ m, and $\xi = z = 0$. The tokamak field is set to $E_l = 0.2$ V/m and $B_0 = 2$ T, and the major radius $R_0 = 1.7$ m.

strength of electric field. Generally speaking, the safety factor q has compound impacts on runaway dynamics, which makes its consequences vague by analyzing any individual factor. During disruptions, large portion of the poloidal magnetic field is induced by the runaway current. So the q profile in major disruption involves self-consistent evolution of runaway electrons. In this part, we use the parameters $E_l = 0.2$ V/m, $B_0 = 2$ T, and $R_0 = 1.7$ m, while the value of q is sampled from 0.2 to 10.

Figure 12 plots the energy limit and the energy balance time against the safety factor q . Both E_{max} and t_{blc} increases as q becomes larger. This phenomenon comes from two main reasons. Firstly, for smaller q , the poloidal field is stronger. Therefore, the toroidal acceleration of electric field is hindered. Secondly, when the toroidal curvature determined by the major radius keeps unchanged, smaller q corresponds to larger poloidal curvature and thus stronger synchrotron radiation. Even though the neoclassical drift velocity is proportional to q and the electric field decreases faster for larger q due to its radial distribution, the numerical results in Fig. 12 imply that the effect of safety factor by modifying the neoclassical

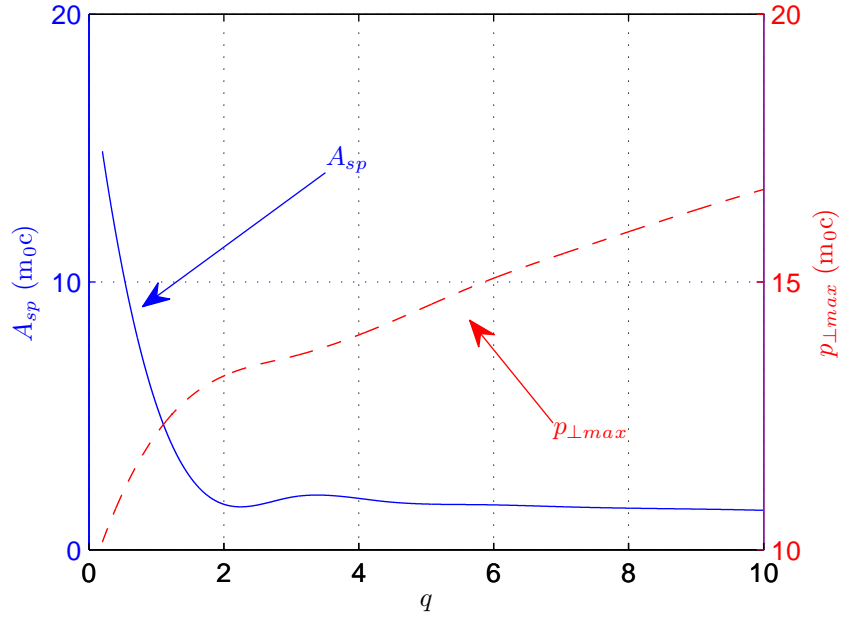


Figure 13. The plots of magnitude of oscillation at energy limit A_{zp} , denoted by the blue solid curve and the left ordinate, and the maximum perpendicular momentum $p_{\perp max}$, denoted by the red dashed curve and the right ordinate, against safety factor. The initial condition of runaway electron in phase space is sampled as $p_{\parallel 0} = 5 m_0c$, $p_{\perp 0} = 1 m_0c$, $R = 1.8$ m, and $\xi = z = 0$. The tokamak field is set to $E_t = 0.2$ V/m and $B_0 = 2$ T, and the major radius is $R_0 = 1.7$ m.

drift is weaker than the above two effects.

The influences of q on collisionless pitch-angle scattering and maximum perpendicular momentum are plotted in Fig. 13. When the safety factor is less than 2, the amplitude of perpendicular momentum oscillation drops evidently with the increase of q . Under this condition, the neoclassical scattering is extremely strong, and it is much easier for an energetic runaway electron to move cross magnetic surfaces. The rotation of magnetic field witnessed by runaway electrons becomes fast at the same time. The oscillation amplitude even exceeds the maximum perpendicular momentum at energy limit when q is small enough. When q is larger than 2, the geometric effects mainly come from the toroidal field. The dependence of A_{zp} on q is not notable. On the other hand, the plot of $p_{\perp max}$ shows the similar trend to that of E_{max} , which increases monotonously with q .

D. Influence of magnetic field ripples on energy limit

In tokamaks, the toroidal magnetic fields are induced by toroidal coils with finite coil number, which leads to magnetic field ripples in experiments. According to L. Laurent and J. M. Rax's paper in 1990, the stochastic instability caused by the nonlinear cyclotron resonances with magnetic field ripples can transfer the parallel energy to perpendicular direction and thus restrict runaway energy limit far below the synchrotron energy limit [42]. In this subsection, utilizing full-orbit simulations, we study the impacts of magnetic field ripples on the runaway energy limit. Besides the equilibrium electromagnetic field given by Eqs. 15 and 16, there also exist the radial perturbation of magnetic ripple $\delta\mathbf{B}$, expressed by

$$\delta\mathbf{B} = \delta B \mathbf{e}_r, \quad (20)$$

$$\delta B(r, \theta, \varphi) = \sum_{m=0, n=1}^{m=\infty, n=\infty} \delta B_{mn}(r) \cos(m\theta) \cos(nN\varphi), \quad (21)$$

where, r , θ , and φ are three components of the toroidal coordinates, N is the number of toroidal field coils, and m and n denote respectively the toroidal and poloidal harmonics. Following the discussion in Ref. [42], we consider only the terms with $m = 0, 1$ in Eq. 21. The amplitude of perturbation magnetic field is given by the analytical approximation for small m , namely,

$$\delta B_{0n}(r) = \delta B_{1n}(r) \approx \frac{B_0}{2} \left(1 + \frac{qR_0}{R_0 + b}\right) \exp\left[-Nn \left(\frac{b-r}{b+R_0}\right)\right], \quad (22)$$

where, b is the radius of toroidal coils. Based on the Tore Supra tokamak [42], we set the simulation parameters as $N = 18$, $B_0 = 1.8$ T, $E_l = 0.1$ V/m, $q = 2$, $R_0 = 2.4$ m, $a = 0.75$ m, and $b = 1.3$ m. The initial condition of the runaway electron is given by $p_{\parallel 0} = 5 m_0 c$, $p_{\perp 0} = 1 m_0 c$, $r_0 = 0.1$ m, and $\theta_0 = \varphi_0 = 0$.

Figure 14 depicts the energy evolution of a runaway electron affected by different harmonics of magnetic ripple. Indicated by the red curve in Fig. 14, without the magnetic field ripple, the synchrotron energy limit is about 80 MeV. When considering the $n = 1$ components of ripple field, δB_{01} and δB_{11} , the maximum runaway energy decreases to about 60 MeV approximately, see the green curve in Fig. 14. The restriction of the $n = 2$ components of ripple field on runaway energy is more significant. As shown by the blue curve, if we add the components of $n = 2$, namely, δB_{02} and δB_{12} , the energy limit is reduced to 22 MeV. The results in Fig. 14 exhibit that the magnetic ripples can limit the maximum runaway energy far below the synchrotron limit, which is consistent with the results in Ref. [42].

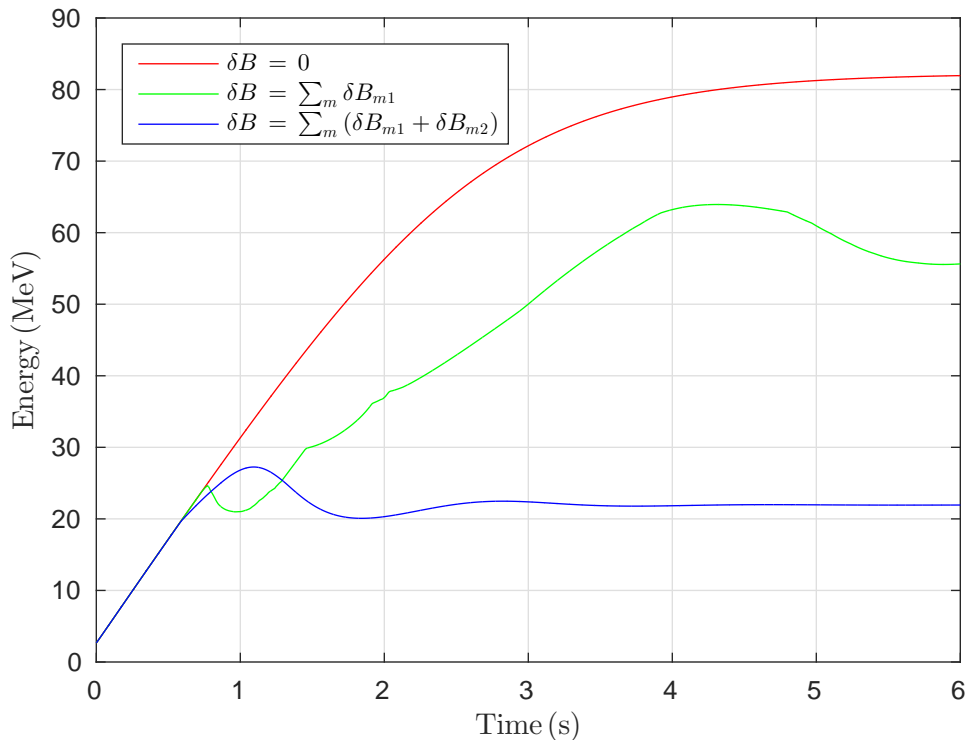


Figure 14. The energy evolution of a runaway electron in tokamak fields with different magnetic ripple perturbations. The red curve shows the energy evolution without magnetic field ripple, the green one depicts the result considering the $n = 1$ components of δB , and the blue one is the result considering both $n = 1$ and $n = 2$ harmonics of δB . The summation over m only covers two lowest components, namely, $m = 0, 1$.

VII. CONCLUSIONS

In this paper, the multi-timescale runaway dynamics in tokamak field is comprehensively exposed. The physical pictures in different timescales, from 10^{-11} s to 3 s, have been fully exhibited. The utilization of the relativistic volume-preserving algorithm is vital to this study, because the long-term numerical accuracy and stability of VPA ensures the accomplishment and correctness of the secular numerical results. In the physical model, the toroidal configuration of tokamak field and the synchrotron radiation are considered. Correspondingly, the key role of geometric effects and coupling of multi-timescale runaway dynamical processes are perfectly captured.

In small timescale imposed by Lorentz force, unlike the common wisdom, the helical

trajectory of energetic runaway electrons is elongated both toroidally and poloidally so much that the collisionless neoclassical scattering rises. A theoretical description of the neoclassical scattering is provided through the coupling between the rotations of magnetic field and momentum. The drift in momentum space is also analyzed based on the rotation vector of magnetic field. The micro timescale dynamics discussed in this paper has established a comprehensive picture of runaway motion. More importantly, our results have shown that the coupling between \mathcal{T}_c and transit period plays an important role for energetic runaways.

In large timescale up to several seconds, the long-term structure of momentum evolution is portrayed by four characteristic quantities. To find out the secular integral laws, we also studied the energy gain-loss ratio and the energy balance time. The initial condition is proved to have significant effects on small timescale momentum oscillation but little influence on the long-term integral behaviors, such as energy limit and energy balance time. Meanwhile, the dynamics of runaways can also be impacted by tokamak parameters. The electromagnetic field, major radius, and safety factor have different influences on both the energy limit and the neoclassical scattering process through altering different aspects of runaway dynamics. It is also proved that the existence of magnetic field ripple can reduce the maximal runaway energy.

Considering the complex influences from many different physical processes in real tokamak discharges, we will study other factors on the energy limit of runaway electrons, such as different instabilities and resonance magnetic perturbations, in the future dynamical analysis of runaway electrons. Meanwhile, the observed runaway effects in experiments are generally collective behaviors of large amounts of runaway electrons. Therefore, the statistical treatment of runaway evolution with large samplings in the phase space will be carried out to obtain macroscopic results, which is convenient for experimental observation and verification.

ACKNOWLEDGMENTS

This research is supported by National Magnetic Confinement Fusion Energy Research Project (2015GB111003, 2014GB124005), National Natural Science Foundation of China (NSFC-11575185, 11575186, 11305171), JSPS-NRF-NSFC A3 Foresight Program (NSFC-

11261140328), and the GeoAlgorithmic Plasma Simulator (GAPS) Project.

- [1] R. Yoshino, T. Kondoh, Y. Neyatani, K. Itami, Y. Kawano, and N. Isei, *Plasma Phys. Control. Fusion* **39**, 313 (1997).
- [2] R. Jaspers, N. L. Cardozo, F. Schuller, K. Finken, T. Grewe, and G. Mank, *Nucl. Fusion* **36**, 367 (1996).
- [3] P. Helander, L.-G. Eriksson, and F. Andersson, *Phys. Plasmas* **7**, 4106 (2000).
- [4] P. Helander, L. Eriksson, and F. Andersson, *Plasma Phys. Contr. Fusion* **44**, B247 (2002).
- [5] T. Fülöp, H. Smith, and G. Pokol, *Phys. Plasmas* **16**, 022502 (2009).
- [6] R. Gill, B. Alper, A. Edwards, L. Ingesson, M. Johnson, and D. Ward, *Nucl. Fusion* **40**, 163 (2000).
- [7] R. Jaspers, K. Finken, G. Mank, F. Hoenen, J. Boedo, N. L. Cardozo, and F. Schuller, *Nucl. Fusion* **33**, 1775 (1993).
- [8] R. Nygren, T. Lutz, D. Walsh, G. Martin, M. Chatelier, T. Loarer, and D. Guilhem, *J. Nucl. Mater.* **241**, 522 (1997).
- [9] P. Parks, M. Rosenbluth, and S. Putvinski, *Phys. Plasmas* **6**, 2523 (1999).
- [10] M. Rosenbluth and S. Putvinski, *Nucl. Fusion* **37**, 1355 (1997).
- [11] R. Yoshino and S. Tokuda, *Nucl. Fusion* **40**, 1293 (2000).
- [12] H. Tamai, R. Yoshino, S. Tokuda, G. Kurita, Y. Neyatani, M. Bakhtiari, R. Khayrutdinov, V. Lukash, and M. Rosenbluth, *Nucl. Fusion* **42**, 290 (2002).
- [13] M. Lehnen, S. Bozhenkov, S. Abdullaev, and M. Jakubowski, *Phys. Rev. Lett.* **100**, 255003 (2008).
- [14] K. Finken, S. Abdullaev, M. Jakubowski, R. Jaspers, M. Lehnen, R. Schlickeiser, K. Spatschek, A. Wingen, and R. Wolf, *Nucl. Fusion* **47**, 91 (2007).
- [15] N. J. Fisch, *Rev. Mod. Phys.* **59**, 175 (1987).
- [16] H. Dreicer, *Phys. Rev.* **115**, 238 (1959).
- [17] J. Connor and R. Hastie, *Nucl. Fusion* **15**, 415 (1975).
- [18] H.-W. Bartels, *Fusion Eng. Des.* **23**, 323 (1994).
- [19] T. Kawamura, H. Obayashi, and A. Miyahara, *Fusion Eng. Des.* **9**, 39 (1989).
- [20] H. Bolt, A. Miyahara, M. Miyake, and T. Yamamoto, *J. Nucl. Mater.* **151**, 48 (1987).

- [21] R. Jaspers, N. L. Cardozo, A. Donne, H. Widdershoven, and K. Finken, *Rev. Sci. Instrum.* **72**, 466 (2001).
- [22] J. Martín-Solís, J. Alvarez, R. Sánchez, and B. Esposito, *Phys. Plasmas* **5**, 2370 (1998).
- [23] J. Martín-Solís, B. Esposito, R. Sánchez, and J. Alvarez, *Phys. Plasmas* **6**, 238 (1999).
- [24] J. Liu, H. Qin, N. J. Fisch, Q. Teng, and X. Wang, *Phys. Plasmas* **21**, 064503 (2014).
- [25] X. Guan, H. Qin, and N. J. Fisch, *Phys. Plasmas* **17**, 092502 (2010).
- [26] J. Liu, Y. Wang, and H. Qin, *Nucl. Fusion* **56**, 064002 (2016).
- [27] M. Bakhtiari, G. Kramer, and D. Whyte, *Phys. Plasmas* **12**, 102503 (2005).
- [28] A. Ware, *Phys. Rev. Lett.* **25**, 15 (1970).
- [29] N. J. Fisch and C. F. Karney, *Phys. Fluids* **24**, 27 (1981).
- [30] H. Qin, X. Guan, and N. J. Fisch, Report No. PPPL-4639, Princeton Plasma Physics Laboratory (PPPL), Princeton, NJ (United States) (2011).
- [31] R. Zhang, J. Liu, Y. Tang, H. Qin, J. Xiao, and B. Zhu, *Phys. Plasmas* **21**, 032504 (2014).
- [32] R. Zhang, J. Liu, H. Qin, Y. Wang, Y. He, and Y. Sun, *Phys. Plasmas* **22**, 044501 (2015).
- [33] Y. He, Y. Sun, J. Liu, and H. Qin, *J. Comput. Phys.* **281**, 135 (2015).
- [34] J. Xiao, J. Liu, H. Qin, and Z. Yu, *Phys. Plasmas* **20**, 102517 (2013).
- [35] H. Qin, S. Zhang, J. Xiao, J. Liu, Y. Sun, and W. M. Tang, *Phys. Plasmas* **20**, 084503 (2013).
- [36] H. Qin and X. Guan, *Phys. Rev. Lett.* **100**, 035006 (2008).
- [37] Y. He, H. Qin, Y. Sun, J. Xiao, R. Zhang, and J. Liu, *Phys. Plasmas* **22**, 124503 (2015).
- [38] Y. He, Y. Sun, J. Liu, and H. Qin, *J. Comput. Phys.* **305**, 172 (2016).
- [39] H. Qin, J. Liu, J. Xiao, R. Zhang, Y. He, Y. Wang, Y. Sun, J. W. Burby, L. Ellison, and Y. Zhou, *Nucl. Fusion* **56**, 014001 (2015).
- [40] J. Xiao, J. Liu, H. Qin, Z. Yu, and N. Xiang, *Phys. Plasmas* **22**, 092305 (2015).
- [41] J. Xiao, H. Qin, J. Liu, Y. He, R. Zhang, and Y. Sun, *Phys. Plasmas* **22**, 112504 (2015).
- [42] L. Laurent and J. Rax, *Europhys. Lett.* **11**, 219 (1990).
- [43] J. D. Jackson, *Classical electrodynamics*, vol. 3 (Wiley New York etc., 1962).
- [44] C. F. F. Karney and N. J. Fisch, *Physics of Fluids* **29**, 180 (1986).
- [45] R. Gill, *Nucl. Fusion* **33**, 1613 (1993).
- [46] O. Jarvis, G. Sadler, and J. Thompson, *Nucl. Fusion* **28**, 1981 (1988).
- [47] K. Wongrach, K. Finken, S. Abdullaev, R. Koslowski, O. Willi, and L. Zeng, *Nucl. Fusion* **54**, 043011 (2014).